On generation of horseshoe vortices by corrugated surfaces, surface roughnesses or pipe bends

N.C. OVENDEN[1] and F.T. SMITH[2]

[1]*Department of Mathematics and Computer Science, Eindhoven University of Technology, P.O. Box 513, 5600 MB Eindhoven, The Netherlands (e-mail: n.c.ovenden@tue.nl)*
[2]*Department of Mathematics, University College London, Gower Street, London WC1E 6BT, United Kingdom*

Abstract. This study is motivated by applications to near-wall shear flow (i) as a longitudinal wall shaping starts, (ii) around a surface obstacle, or (iii) through a pipe bend. All are shown to be governed, at relatively high flow rates, by essentially the same theoretical problem. This concerns three-dimensional nonlinear longitudinal vortex-like motion under a prescribed displacement which continues to increase with distance downstream. Symmetry-plane solutions are obtained mainly through forward marching computation followed by analysis of the far-downstream response. The behaviour far downstream is found to involve either a strengthening attachment or an increasing three-dimensional separation (lift-off) with no backflow.

Key words: bend, corrugation, horseshoe vortices, roughness, slender flow, three-dimensional.

1. Introduction

The motivation for the present study comes from three main fluid-flow applications, described as (i) to (iii) below, all of which involve the generation of longitudinal vortices in reality and are found to lead to essentially the same mathematical problem. These are on a near-wall shear flow: (i) as a longitudinal shaping of the wall begins (there is practical interest in streamwise corrugated-surface effects ahead of a trailing edge), (ii) around a surface obstacle (*e.g.*, a roughness element) and (iii) through a pipe bend. More generally, (i) covers the start of any dent and/or rise in the surface shape, and (ii) covers the flow skirting around the side of any highly pressurised area.

Background experiments, visualisation, theory and computations for (i) to (iii) can be found in [1–10]. The generation or mechanisms of strong horseshoe vortices remain largely unexplained physically, despite numerous computational and other results.

Here we investigate steady laminar three-dimensional motion at large Reynolds numbers. Section 2 describes the contexts (i) to (iii) in greater detail and their common governing equations, which correspond to a nonlinear vortex system with an imposed displacement that amplifies downstream. Solutions are derived numerically in Sections 3 and 4 for symmetry-plane flow with varying degrees of either increasing or decreasing displacement. The analysis in Section 5 then concentrates on the flow properties far downstream. Further comments and a discussion are presented in Section 6, including note of other applications.
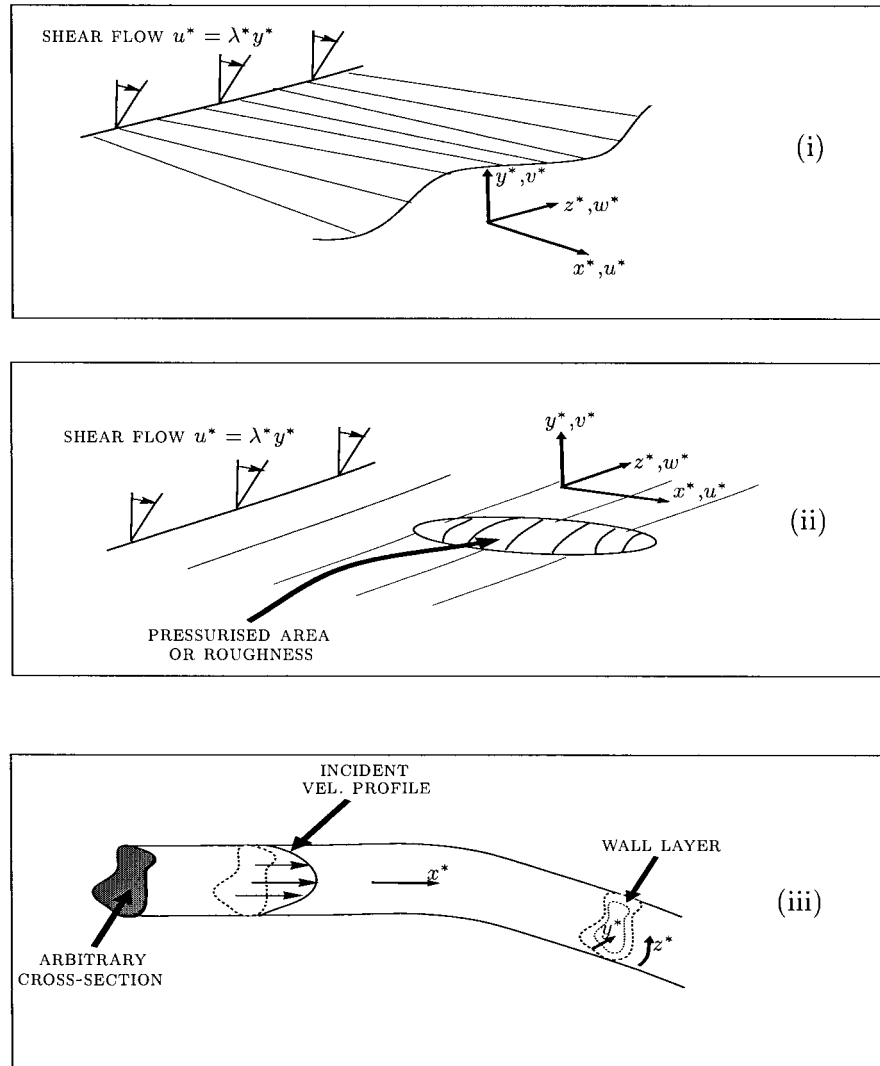
Figure 1. The three main applications that involve the generation of longitudinal vortices: (i) as a longitudinal wall shaping begins, (ii) around a surface obstacle or pressurised area and (iii) through a pipe bend.

2. The physical problems and governing equations

The three main applications of this work are to (i) the shear flow near the start of a gradual longitudinal dent or hump on a solid wall (*e.g.* as on a corrugated surface), (ii) the motion induced to the side of a surface-mounted obstacle and (iii) the flow through a bent or cornered pipe. See Figure 1.

The application (i) is described in terms of Cartesian coordinates x^*, y^*, z^*, representing the streamwise, normal and spanwise directions, respectively, and the corresponding velocity components u^*, v^*, w^*. The wall shape of concern is assumed to lie deep inside the surface boundary layer (or other oncoming shear flow) and is so localized that the undisturbed surface appears flat and of indefinite length (in the x^*-z^* plane). The fluid appears to be of semi-infinite extent in the normal direction, with a uniform incident shear flow $u^* = \lambda^* y^*$, where

λ^* is the prescribed slope of the incident velocity profile at the surface. The only geometric length scales of direct relevance are those imposed by the wall shaping itself. We take typical streamwise and spanwise distances L^* and l^* of the wall shaping as the characteristic length scales for x^* and z^*, respectively. Similarly, as there is no velocity scale implied directly we choose the characteristic velocity scale to be λ^* multiplied by l^*. The associated Reynolds number based on the near-wall flow field is chosen as $\text{Re}_w \equiv (\lambda^* l^*) \, l^*/\nu^*$, where ν^* is the kinematic viscosity of the incompressible fluid, the density of which is ρ^*. Here Re_w is assumed to be large.

Suppose that the wall shaping is closely aligned with the incident shear flow, in the sense that $l^* \ll L^*$, and that the typical height variation is given by f^*. Such alignment is expected to provoke an interaction between the incident shear motion, which emphasises the streamwise direction, and the most rapid shape variation, which is in the spanwise direction. Close to the surface, a three-dimensional viscous layer is induced, of y^* scale $(\nu^* L^*/\lambda^*)^{1/3}$ from the inertial/viscous balance of $u^* \partial/\partial x^*$ $(\sim \lambda^* y^*/L^*)$ against $\nu^* \partial^2/\partial y^{*2}$ $(\sim \nu^*/y^{*2})$. The layer is also nonlinear, thus allowing for three-dimensional separations for example, provided that the viscous y^* scale derived above is comparable with $|f^*|$. Hence the wall shape has f^* prescribed as $\delta^* B(x, z)$, where $\delta^* = (l^{*2} L^*/\text{Re}_w)^{1/3}$, $y^* = \delta^*(y + B)$, while $[u^*, v^*, w^*]$ is $\lambda^* \delta^* \left[L^* u, \delta^*(v + u B_x + w B_z), l^* w \right]/L^*$ and the dimensional pressure p^* is written as $\rho^* (\lambda^* \delta^* l^*/L^*)^2 p$. The viscous layer is thin provided that $(\nu^* L^*/\lambda^*)^{1/3} \ll l^*$, i.e., (l^*/L^*) is much greater than Re_w^{-1}. Indeed, all the physical assumptions implicit above are valid as long as the length-to-width ratio of the wall shaping is much greater than Re_w^{-1}, but still small. The viscous wall layer is then controlled by the nonlinear wide-vortex or slender three-dimensional boundary-layer system, in nondimensional form,

$$\frac{\partial u}{\partial x} + \frac{\partial v}{\partial y} + \frac{\partial w}{\partial z} = 0, \tag{1}$$

$$\left(u \frac{\partial}{\partial x} + v \frac{\partial}{\partial y} + w \frac{\partial}{\partial z} \right) u = 0 + \frac{\partial^2 u}{\partial y^2}, \tag{2}$$

$$\left(u \frac{\partial}{\partial x} + v \frac{\partial}{\partial y} + w \frac{\partial}{\partial z} \right) w = -\frac{\partial p}{\partial z} + \frac{\partial^2 w}{\partial y^2}, \tag{3}$$

with the unknown pressure term $p(x, z)$ being independent of Y due to the normal momentum balance. The streamwise pressure gradient is negligible because of the different velocity scales u^*, w^* inferred from the continuity balance. The boundary conditions here are

$$u \sim y + B(x, z) \qquad \text{as} \quad y \to \infty, \tag{4}$$

$$w \propto y^{-1} \qquad \text{as} \quad y \to \infty, \tag{5}$$

$$u = v = w = 0 \qquad \text{at} \quad y = 0, \tag{6}$$

$$(u, v, w, p) \to (y, 0, 0, 0) \quad \text{as} \quad x \to -\infty, \tag{7}$$

from matching with the outer flow solution, from the no-slip constraint and from merging with the undisturbed incident shear flow far upstream at fixed z, respectively. Condition (4) is, in fact, that of zero outer displacement (in other words, condensed flow [12, 12]) because of the

Prandtl-transposition coordinate $(y + B)$. In (1) to (7), the scaled velocity components u, v, w are unknown functions of x, y, z and the scaled induced surface pressure $p(x, z)$ is to be found, whereas the negative displacement (or forcing) function $B(x, z)$ is prescribed.

The application (ii), to flow beside an obstacle or, more generally, beside an area of typical dimensional pressure variation π^* say, stems from [6, 7], the latter paper suggesting it as an origin for horseshoe vortices. Next to the area of imposed pressure (of length scales L^*, l^* again) the largest distinct region has $y^* \sim l^*$ and there an inviscid three-dimensional linearisation of the incident shear flow applies, with the induced streamwise pressure gradient again being negligible. The constraints on the motion are that as the surface is approached the pressure perturbation is prescribed within the pressurised area, and zero around it, while at sufficiently large distances the pressure perturbation decays to zero. The normal velocity component is also zero at the surface outside the pressurised area, whereas the streamwise and spanwise components are nonzero in general, yielding a slip velocity there. The flow solution [7] there gives the result

$$\frac{\partial^2 B}{\partial x^2} = -\frac{1}{\pi}(\mathrm{PV}) \int_{-\infty}^{0} \frac{\partial^3 \tilde{\pi}(x, \eta)}{\partial \eta^3} \frac{\mathrm{d}\eta}{(z - \eta)} \tag{8}$$

for the double streamwise derivative of the scaled streamwise slip velocity B, where (PV) denotes the principal value and the scaled imposed pressure $\tilde{\pi}$ ($\propto \pi^*$) is supposed to decay sufficiently fast upstream as $x \to -\infty$ for z fixed. Closer to the flat surface the viscous layer provoked by the induced slip velocity $B(x, z)$ then satisfies (1) to (7) exactly.

The change in role of B, from a prescribed slip velocity produced in the outer inviscid region to a prescribed displacement effect in the inner viscous sublayer, is the three-dimensional companion of the change described in [13] and, as there, it arises because of the pre-existing linear velocity profile as opposed to a uniform profile near the surface. The change is significant in that it allows the surface pressure p to adjust and, in particular, any flow reversals are encountered in a regular fashion rather than with a classical singularity; the same comment applies to the other applications (i) and (iii). On top of this, for application (ii), the maximum influence of the imposed pressure $\tilde{\pi}$ on the flow next to the pressurised area tends to come at first from positions of enhanced $\tilde{\pi}$ variation, particularly through high values of the third derivatives of $\tilde{\pi}$ in the *spanwise* direction. However, this is countered by the property that a double *streamwise* integration is required to obtain the displacement B itself. This last property indicates an immediate and substantial *historical influence* in the motion (ii), due to (8), an influence which is absent in the other two applications (although distinct historical effects common to all three applications are discussed later). These enhanced spanwise and streamwise influences, in the pressure-feedback mechanism from the pressurised area, are three-dimensional features which are distinct from those examined previously and arise essentially from the near-alignment of the incident near-surface shearing motion with the longitudinal edge of the pressurised area.

When the pressurised area is a low obstacle on the surface, [7] shows how $\tilde{\pi}(x, z)$ is determined by the complex flow behaviour on the obstacle; see also [6] and Appendix A. The forcing B then follows from (8). Below we will examine representative B functions which typically grow linearly far downstream and so allow for the effect of the derivatives in (8).

The application (iii) is very similar to (i). This is due to equations (1) to (3) applying in a relatively thin layer near the solid surface, which is the inner wall of the pipe in the case of (iii). With x defined as the axial distance down the pipe, (4) and (5) follow from

applying the Prandtl transposition again to the pipe bend. Periodicity in z, *i.e.*, around the pipe cross-section, is required however here.

All the applications, then, essentially yield the same problem (1) to (7). The negligible influence of the streamwise pressure gradient in (2), *e.g.*, due to the slender wall shape, causes the wall-layer system to be parabolic in the positive streamwise direction provided that u remains positive. The following work addresses the flow properties in a symmetry plane. The physical relevance of this is clear in the applications (i) and (iii), whereas for (ii) it serves more as a guideline to the possible realistic flow features.

3. Symmetry-plane analysis

For guidance, we examine the solution close to a symmetry line. Thus, for small z, the expressions

$$[u, v, w, p, B] = \left[U(x, y), V(x, y), zW(x, y), \frac{z^2}{2} P(x), A(x) + \frac{z^2}{2} A_2(x) \right] + \dots \tag{9}$$

are expected, where $A(x)$ and $A_2(x)$ etc. are *known*, with the additional property that

$$A(x) \sim \sigma x \quad \text{as } x \to \infty, \tag{10}$$

for a given constant σ. The property (10) corresponds to an imposed displacement (a corrugation, a roughness-induced slip via (8) or a pipe bend) with amplitude that increases indefinitely downstream. Substituting in (1) to (7) then yields the symmetry-line equations

$$\frac{\partial u}{\partial x} + \frac{\partial V}{\partial y} + W = 0, \tag{11}$$

$$U \frac{\partial u}{\partial x} + V \frac{\partial U}{\partial y} = \frac{\partial^2 U}{\partial y^2}, \tag{12}$$

$$U \frac{\partial W}{\partial x} + V \frac{\partial W}{\partial y} + W^2 = -P(x) + \frac{\partial^2 W}{\partial y^2}, \tag{13}$$

to leading order, with boundary conditions

$$(U, V, W, P) = (y, 0, 0, 0) \quad \text{at } x \leqslant 0, \tag{14}$$

$$(U, V, W) = (0, 0, 0) \quad \text{at } y = 0, \tag{15}$$

$$(U, W) \sim \left(y + A(x), O(y^{-1}) \right) \quad \text{as } y \to \infty. \tag{16}$$

Despite the simplifications, the solution to the nonlinear symmetry-line problem (11) to (16) must still be found numerically. The parabolic nature of the governing equations enables the solution to be marched forward in the x-direction (so long as no flow reversal occurs) and, here, a quasi-linear iterative process is used to determine the values at successive streamwise locations. Resolving the flow field is made difficult by the linearly growing slip velocity (16), which necessitates a large grid in the y-direction, and the absence of a streamwise pressure gradient, which creates only a loose coupling between the slip velocity and unknown pressure.
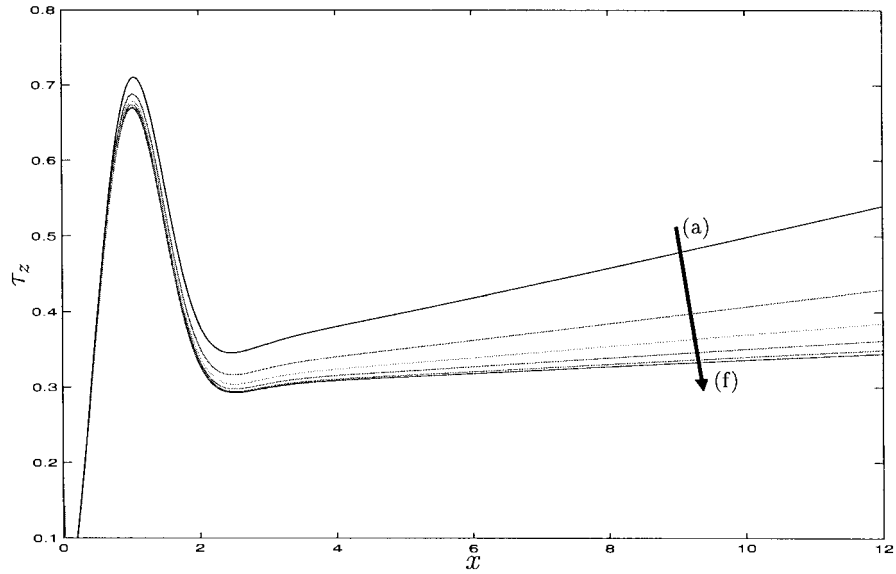
Figure 2. Spanwise skin friction for the case $\sigma = +0.5$, where the $y \to \infty$ boundary condition is imposed at different maximum y values. For each plot shown this boundary condition is imposed at (a) $y_{max} = 15.7$, (b) $y_{max} = 29.5$, (c) $y_{max} = 47.8$, (d) $y_{max} = 71.2$, (e) $y_{max} = 98.0$ and (f) $y_{max} = 115.2$. The arrow shows the trend of increasing y_{max}.
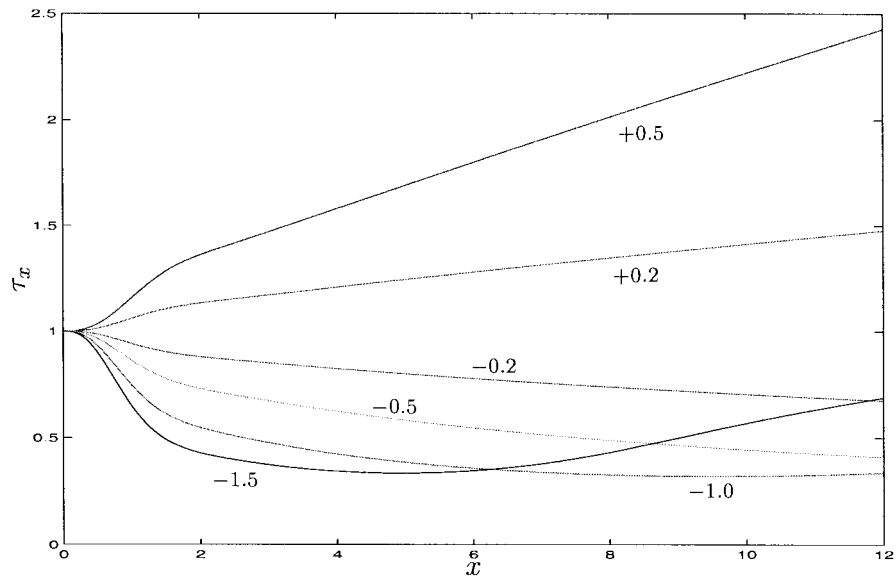

Figure 3. Streamwise skin friction on the symmetry line for different values of σ as labelled.

So, a stretched grid $y = \gamma e^{\Omega \bar{y}} - \gamma$ is employed to capture the algebraic decay of W and to enable (16) to be imposed at a suitably large y. Some solutions are strongly dependent on grid height y_{max} and grid spacing; the parameters γ and Ω are used to control near-wall and far-field grid spacings.
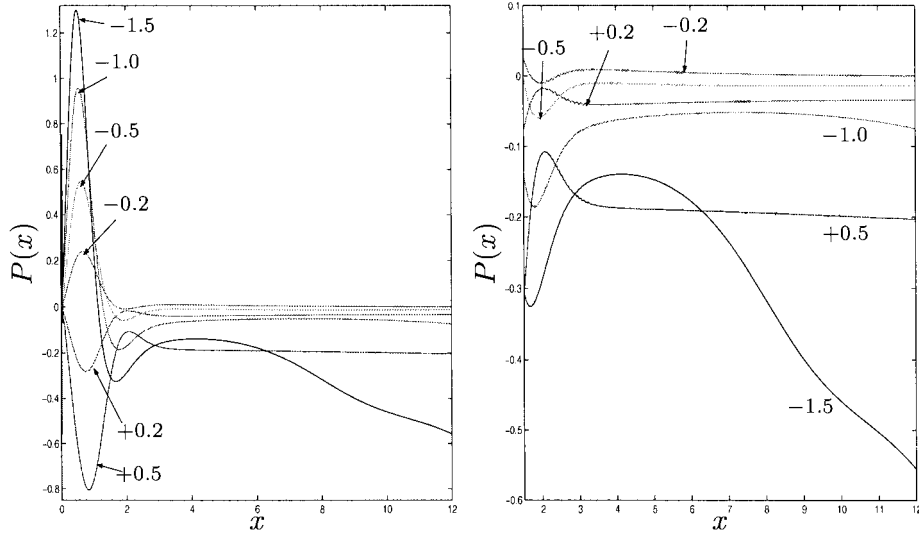
Figure 4. The symmetry-line pressure contribution $P(x)$, which dictates the induced spanwise pressure gradient, for different values of σ as labelled.
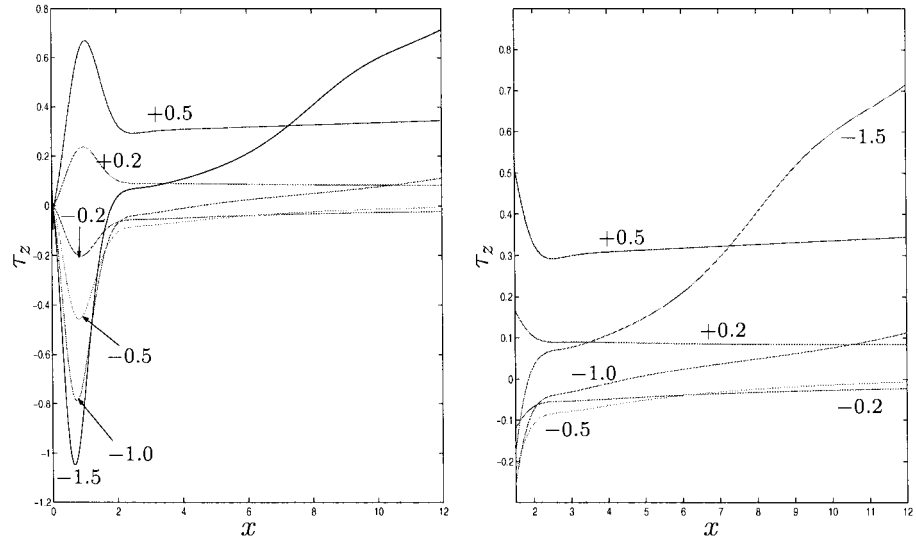

Figure 5. The symmetry-line spanwise skin friction behaviour for different values of σ as labelled.

4. Numerical results

The numerical scheme was used with the slip-velocity

$$A(x) = \sigma x \left(1 - e^{-x^2}\right),$$

which provides a necessary smooth start in the vicinity of $x = 0$ (see Appendix B) but tends rapidly to the required asymptote (10). Numerical results for various values of σ are presented in Figures 2 to 6. The results contain plots of the scaled streamwise skin friction $\tau_x = \partial U/\partial y\big|_{y=0}$, the scaled spanwise skin friction $\tau_z = \partial W/\partial y\big|_{y=0}$, the pressure $P(x)$ and the downstream streamwise and spanwise velocity profiles. Grid checks show that results for
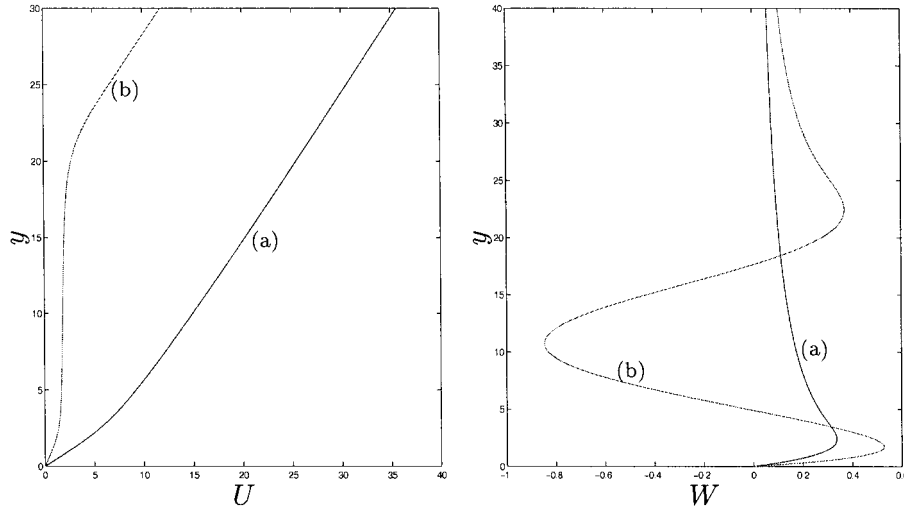
Figure 6. Downstream streamwise and spanwise velocity profiles computed on the symmetry line at $x = 12$ for (a) $\sigma = +0.5$ and (b) $\sigma = -1.5$.

the larger values of σ positive are strongly dependent on $y_{\max}$. The effect can be observed in Figure 2, where τ_z is computed for $\sigma = +0.5$ with the $y \to \infty$ condition (16) imposed at different $y_{\max}$ values. For smaller values of $y_{\max}$ the near-wall spanwise velocity appears to be increasing in strength far downstream. However, as $y_{\max}$ is increased, τ_z seems to approach a constant value, in agreement with the asymptotic analysis of the next section. By adjusting the grid parameters γ and Ω to make the grid height as large as computationally possible (whilst maintaining a fine enough grid at the wall), these grid effects are minimised in all the other results presented.

For the cases where $\sigma > 0$, the initial smooth growth of the slip velocity is unable to prevent the almost immediate creation of a sharp favourable pressure gradient in the direction of large $|z|$. This pressure gradient, in turn, induces an equally large spanwise acceleration of near-wall fluid outwards *away from the symmetry line* at $z = 0$, a feature observable in Figure 5. As x increases further and $A(x)$ attains its asymptotic form (10), the pressure gradient weakens slightly before appearing to level out at an almost constant value as the flow proceeds further downstream. As mentioned above, Figure 5 indicates that τ_z also tends to approach a constant value. The streamwise skin friction in Figure 3 rises steadily as the slip velocity increases, leading to a strongly attached velocity profile downstream as expected (Figure 6). The growth of the streamwise skin friction appears slightly slower than linear.

When $\sigma < 0$ we should perhaps expect reversal of the near-wall fluid downstream. The dependence on $y_{\max}$ is much less here, incidentally, and this can be explained by comparing (see Section 6) the asymptotic structures of both attached and separated cases derived in the next section. In accordance with linear theory (Appendix B), close to $x = 0$ a sharp adverse pressure gradient in the direction of large $|z|$ appears, which pulls fluid inwards spanwise *towards the symmetry line*. Together with that, the streamwise skin friction in Figure 3 begins to drop smoothly as if anticipating separation. However, this initial behaviour does not persist far downstream, as within an $O(1)$ distance from the origin, fully nonlinear effects for the larger $|\sigma|$ cases change the character of the flow response entirely. For instance, the original sharp adverse pressure gradient weakens sharply before becoming instead a modest favourable
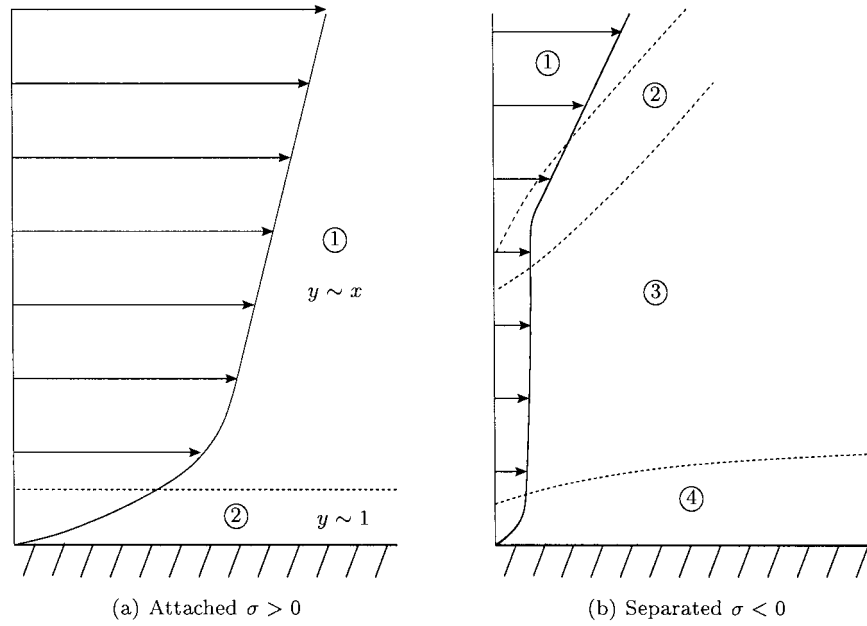
(a) Attached $\sigma > 0$ (b) Separated $\sigma < 0$

Figure 7. Sketch of the flow structure far downstream with the various flow regions labelled.

pressure gradient in the direction of large $|z|$. This favourable pressure gradient continues far downstream and abruptly decelerates the spanwise influx of fluid towards the symmetry line. For the $\sigma = -1 \cdot 0$ and $-1 \cdot 5$ cases, the deceleration is so strong that eventually the spanwise flow reverses close to the surface (Figure 5) and near-wall fluid begins to be expelled outwards *away from the symmetry line*. The streamwise skin friction in Figure 3 at this point stops decreasing and even begins to rise again at larger values of x, suggesting that streamwise *flow reversal never occurs* downstream, despite the linearly decreasing slip velocity; *separation*, in the sense of lift-off, does occur however. For the strongest separated case, $\sigma = -1 \cdot 5$, the streamwise velocity in Figure 6 starts to take the form of an increasingly detached sharply inflected profile that nevertheless has no flow reversal at all. The respective spanwise velocity profile W with its two changes in sign, and an examination of the vertical velocity (not shown here), suggest the formation of vortical structures lifting off downstream for the strong $\sigma < 0$ cases.

5. Far-downstream analysis

The flow structure far downstream is assumed initially to consist of two regions: an outer inviscid region (region 1) and an inner viscous region below (region 2). A diagram is shown in Figure 7(a).

Region 1 is assumed to grow in height linearly as $x \to \infty$ in order to balance the two components of the outer boundary condition $U \sim y + \sigma x$. So, we change coordinates from (x, y) to (x, η), where $\eta = y/x$, and write

$$[U, V, W, P] = \left[x U_0(\eta), x V_0(\eta), W_0(\eta), q_0 \right] + \dots . \tag{17}$$

The leading-order powers of x are chosen to fit condition (16) and to balance terms in (11) to (13); thus we ensure a fully three-dimensional response. Substitution in the governing equations produces the following inviscid system to leading order,

$$U_0(\eta) - \eta U_0'(\eta) + V_0'(\eta) + W_0(\eta) = 0, \tag{18}$$

$$U_0(\eta) \left[U_0(\eta) - \eta U_0'(\eta) \right] + V_0(\eta) U_0'(\eta) = 0, \tag{19}$$

and

$$-\eta U_0(\eta) W_0'(\eta) + V_0(\eta) W_0'(\eta) + W_0^2(\eta) = -q_0. \tag{20}$$

The no-slip conditions from (15) are to be satisfied in region 2 below. In region 1, only the outer conditions (16), along with the no-penetration condition for V_0 at the surface from (15) apply, requiring

$$(U_0, W_0) \sim (\eta + \sigma, 0) \quad \text{as } \eta \to \infty, \tag{21}$$

and

$$V_0 = 0 \quad \text{at } \eta = 0. \tag{22}$$

To solve, first we eliminate V_0 and W_0 using (18) and (19) to express them in terms of U_0. Thus,

$$V_0 = -\frac{U_0^2}{U_0'} + \eta U_0 \quad \text{and} \quad W_0 = -\frac{U_0^2 U_0''}{(U_0')^2}. \tag{23}$$

Then, substitution in (20) and putting $H(t) = \mathrm{d}U_0/\mathrm{d}\eta$, $t = 1/U_0$ (assuming U_0 is a monotonically increasing function of η), gives the equation

$$\frac{\mathrm{d}^2 H}{\mathrm{d}t^2} + q_0 H = 0. \tag{24}$$

Hence, there is an eigenvalue problem to solve for the pressure term q_0. Any solution for $q_0 > 0$, which satisfies (21), has the restriction that U_0 must tend to a constant at $\eta = 0$, yielding $V_0 \neq 0$ at $\eta = 0$ from (23) and violating (22). Therefore, $q_0 \leqslant 0$. Applying (21) then leads to

$$U_0'(\eta) = \cosh\left(\frac{|q_0|^{1/2}}{U_0(\eta)} \right), \tag{25}$$

as the solution to region 1, with a single arbitrary parameter $|q_0|$.

5.1. INCREASINGLY ATTACHED: $\sigma > 0$

For the case of increasingly attached flow, the pressure term q_0 can be fixed uniquely. The no-penetration condition (22) requires from (23) that $U_0 \to 0$ as $\eta \to 0$, other forms being unmatchable. Hence, q_0 is determined by the integral equation

$$\int_0^\infty \left(1 - \frac{1}{\cosh\left(\frac{|q_0|^{1/2}}{U_0(\eta)} \right)} \right) \mathrm{d}U_0 = \sigma. \tag{25}$$
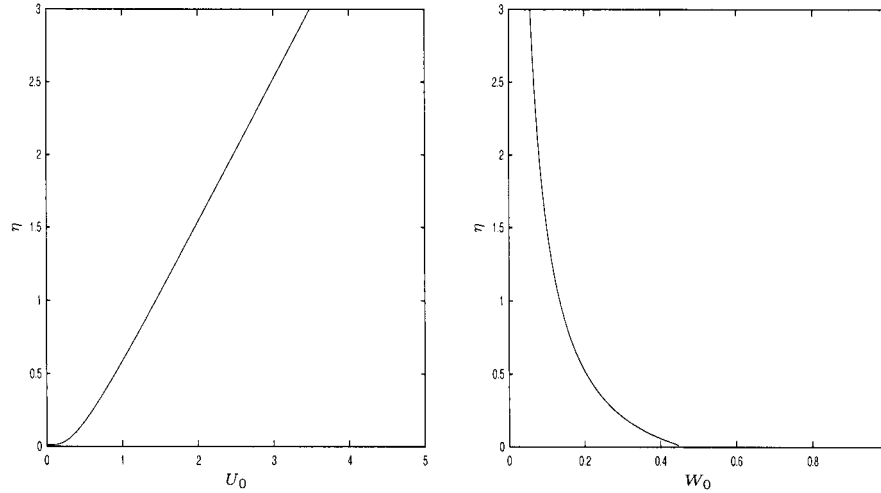
Figure 8. Asymptotic profiles $U_0(\eta)$ and $W_0(\eta)$ predicted for the $\sigma = +0\cdot5$ case.

Calculating the solution to this integral equation numerically for $\sigma = 0\cdot2$ yields the value $q_0 = -0\cdot033$ and for $\sigma = 0\cdot5$ yields the value $q_0 = -0\cdot20$ to two significant figures, which agree encouragingly with the forward marched solution of the pressure term (Figure 4).

Also, from (23) and (25),

$$W_0 = |q_0|^{1/2} \tanh\left(\frac{|q_0|^{1/2}}{U_0}\right). \tag{27}$$

Figure 8 shows the U_0 and W_0 asymptotic profiles calculated for $\sigma = 0\cdot5$.

The viscous region 2 underneath can be shown [14, Chapter 7] to have constant thickness, $y \sim O(1)$, with the expansions

$$[U, V, W, P] = \left[\frac{x}{\log x}\hat{u}(y) , \hat{v}(y) , \hat{w}(y) , -q_0\right] + \ldots . \tag{28}$$

Here, the secondary velocities V and W dominate the flow field, the streamwise leading-order flow being smaller by a factor $O(1/\log x)$. From substitution of (28) in (11) and (13), V and W satisfy the well-known equations governing steady viscous flow approaching a forward stagnation point [15, pp. 231–233]. Moreover, the leading-order streamwise velocity predicts that the streamwise skin friction τ_x grows at a slower rate than linear, namely as $O(x/\log x)$ at large x, in agreement with the behaviour observed in the numerics (see Figure 3).

5.2. INCREASINGLY SEPARATED: $\sigma < 0$

The two-layered structure above fails in the case $\sigma < 0$. Instead, four zones are involved. A sketch of the new structure is given in Figure 7(b).

In region 1, where $\eta = y/(|\sigma|x) > 1$, consideration of (25) implies that $q_0 = 0$ and the solution becomes two-dimensional to leading order,

$$[U, V, W, P] = \left[|\sigma|x(\eta - 1), |\sigma|^2 x(\eta - 1), 0, 0\right] + \ldots . \tag{29}$$

Thus, both the pressure and spanwise flow decay as $x \to \infty$, unlike in the increasingly attached case where they remain constant far downstream.

As the position $y = |\sigma|x$ is approached, there is a dramatic change in vorticity between the inviscid solutions in regions 1 and 3, which is smoothed out by the action of viscous forces [16, 17] within region 2. There $y = |\sigma|x + x^{1/3}\zeta$, with $\zeta \sim O(1)$ and

$$[U, V, W, P] = \left[x^{1/3}F(\zeta), |\sigma|x^{1/3}F(\zeta) + x^{-1/3}G(\zeta), x^{-2/3}H(\zeta), x^{-4/3}\hat{q}\right] + \dots . \quad (30)$$

Substitution in (11) to (13) then produces the system

$$\frac{1}{3}\left[F - \zeta F'\right] + G' + H = 0, \quad \frac{F}{3}\left[F - \zeta F'\right] + GF' = F'',$$

$$-\frac{2}{3}FH - \frac{1}{3}\zeta FH' + GH' + H^2 = -\hat{q} + H'', \quad (31)$$

with the upper condition

$$F(\zeta) \sim \zeta \quad \text{as } \zeta \to \infty, \quad (32)$$

to match to the solution in region 1. The lower condition as suggested by the detailed analysis of [14, Chapter 7] is

$$[F(\zeta), G(\zeta), H(\zeta)] \sim \left[\frac{3|\hat{q}|^{1/2}}{\log|\zeta|}, -|\hat{q}|^{1/2}|\zeta|, -|\hat{q}|^{1/2}\right] + \dots , \quad (33)$$

indicating that the G-term *overtakes* the F-term in the expansion for V (30) inside the shear layer. So the streamwise velocity U, on approaching region 3 becomes negligible by a factor $O(1/\log x)$, resulting in a flow field dominated below the shear layer by the secondary velocities V and W.

In the second inviscid region, region 3, the domain is $0 < \eta < 1$ and the expansions

$$[U, V, W, P] = \left[\frac{x^{1/3}}{\log x}\tilde{U}(\eta), |\sigma|x^{1/3}\tilde{V}(\eta), x^{-2/3}\tilde{W}(\eta), x^{-4/3}\hat{q}\right] + \dots \quad (34)$$

hold. These expansions, when substituted in (11) to (13), confirm that the secondary velocities V and W just dominate the solution here, leaving the balances

$$\tilde{V}' + \tilde{W} = 0, \quad \tilde{V}\tilde{W}' + \tilde{W}^2 = |\hat{q}|. \quad (35)$$

The matching to region 2 above requires $\tilde{V}(\eta) \sim +|\hat{q}|^{1/2}(\eta - 1)$ and $\tilde{W}(\eta) \sim -|\hat{q}|^{1/2}$ as $\eta \to 1-$; the solution obtained has

$$\tilde{V}(\eta) = -\frac{|\hat{q}|^{1/2}}{\pi}\sin(\pi\eta), \quad \tilde{W}(\eta) = |\hat{q}|^{1/2}\cos(\pi\eta). \quad (36)$$

This predicts one change of sign occurring in the spanwise velocity, which is in keeping with that observed in the downstream numerics (Figure 6); any other change of sign presumably occurs either in the shear layer or in the higher-order solutions to region 1.

On approaching the wall at $\eta = 0+$, the flow solution (36) takes the form

$$\tilde{V} \sim -|\hat{q}|^{1/2}\eta \quad \text{and} \quad \tilde{W} \sim |\hat{q}|^{1/2}; \quad (37)$$

fluid is now being pushed downwards and *outwards* from the symmetry line. Viscous forces become significant in a wall layer of thickness $O(x^{1/3})$, defining region 4. There, as in the
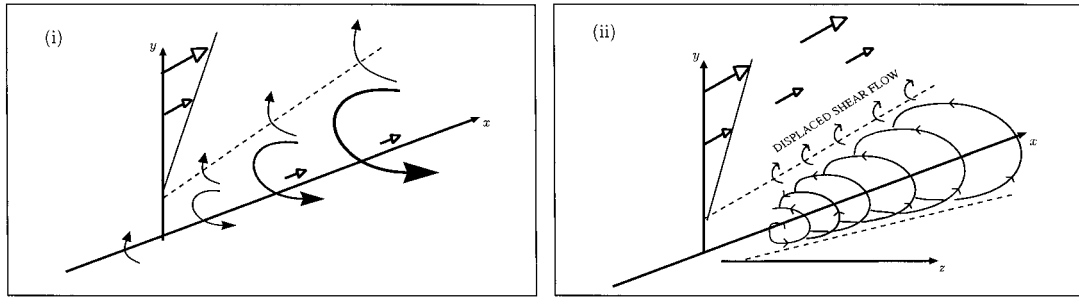
Figure 9. Sketch indicative of the predicted longitudinal vortex flow downstream, when the constant σ is negative. (i) Near symmetry plane $z = 0$, the velocity vectors in the cross plane (solid-headed arrows) and in the x-direction (open-headed arrows): note that all are directed forward in x. (ii) More widely in z, the implied particle paths, especially between the displaced shear flow and the wall. All particles move forward in x. The size of the vortex in the cross-section increases linearly with downstream distance x (indicated by the dashed lines).

attached case, the equations modelling flow towards a forward stagnation point [15, pp. 231–233] apply. Regarding the behaviour of the streamwise velocity below the shear layer, *U remains positive* and satisfies a linear equation in region 4 which, under the action of viscosity, reduces the velocity smoothly to zero at the wall.

6. Further comments

Connections between the asymptotics (Section 5) and numerics (Section 4) need mentioning first. For *increasingly attached* flows, where the slip velocity increases linearly, there is encouraging agreement between the computations and the downstream asymptotic structure. Difficulties due to strong grid dependence (Section 4) prevent further comparisons involving cases where $\sigma > 0.5$. The cause of these difficulties is evident in the asymptotic structure, where clearly a grid height $y_{\max} \gg O(\sigma x)$ is required to satisfy the outer boundary condition (16), with the downstream asymptote (10), to any suitable degree of accuracy. In any case, the analysis indicates that far downstream a strongly attached streamwise flow is formed which, in turn, generates a constant favourable spanwise pressure gradient and a constant spanwise mass flux outwards from the symmetry line. Historical effects on the flow are dissipated in higher-order eigensolutions.

In the *increasingly separated* cases, where the slip velocity decreases linearly, agreement between the asymptotic structure and the computations exists, although it is less obvious. Indeed, the asymptotics predict less dependence on grid height in this case due to the fact that the outer boundary condition downstream, given by (16) with (10), is satisfied to leading order directly above the shear layer ($y \sim |\sigma| x$); in other words, an accurate numerical result can be expected if the grid height $y_{\max}$ lies above this shear layer for all resolved x. The computations fail to resolve the flow sufficiently far downstream for the expansion terms in the asymptotic structure of Section 5 to become significantly different in magnitude. For instance, the factor $O(1/\log x)$ makes numerical confirmation of the asymptotics a challenging future problem. Again, questions remain on the uniqueness of the pressure and the effects of flow history. The absence of backflow in this three-dimensional separation or lift-off is, however, most noteworthy.

Horseshoe Vortices. The numerical and asymptotic approaches together tend to confirm the existence of a complex flow structure far downstream, with the formation of a pair of

horseshoe-type vortices (vortical structures) being a likely feature of the flow. This is evident both in the numerical description at the end of Section 4 and in the asymptotic solution for region 3, in Section 5, which generates a pair of linearly growing horseshoe-type vortices between the wall and the lifting-off shear layer. Of course this is *tentative*, as only a symmetry-line solution has been explored in the present work. A further numerical computation for z of $O(1)$ beyond the symmetry line would be required to fully confirm their existence (see Figure 9). Meanwhile, it is worth noting again the applications (Section 2 and Figure 1) to the three main configurations given in the title of this paper, for each of which downstream horseshoe vortex generation is predicted. On the application (ii), examples of other pressurised configurations concern flow around an entire three-dimensional obstacle, motion beside a floating body, branching flow, motion induced by a suction or injection hole and two-fluid configurations such as at the side of a lake. The flow within the pressurised area may be complex, but the nature of the relation (8) allows fairly representative forcings B to be deduced. The result (8) also matches back to [6]'s quasi-planar work (their Equation 5.7d) upstream around an obstacle. On the application (iii), the ability to control the strength of the horseshoe vortices, through the design of a pipe junction for example, is of great interest. This control may be possible if the leading-order pressure contribution $\hat{q}x^{-4/3}$ present far downstream is not determined uniquely for the separated $\sigma < 0$ cases (unlike for the cases $\sigma > 0$).

Acknowledgement

Appendix A: Further points on flow due to an obstacle

If the obstacle or roughness has steep edges [6] with an extensive flat top, then the flow over it is of most interest at the spanwise outermost edge where there is near-alignment with the incident shear motion. The flow above this edge is nonlinear and two-layered in the normal direction y^*, for the application (ii), whereas on the flat top surface the flow is single-layered but is aware only of the change in surface height, not of the detailed edge shape. The outer layer has a characteristic pressure level π^* and the spanwise velocity w^* is of order $(\pi^*/\rho^*)^{1/2}$. So conservation of mass suggests that u^* is represented by $(\pi^*/\rho^*)^{1/2}L^*/l^*$. Comparing this with the representative value $\lambda^* y^*$ due to the incident shear flow fixes the y^* thickness scale as $(\pi^*/\rho^*)^{1/2}L^*/(l^*\lambda^*)$. The same scale is expected for the typical roughness height F^* at the steep edge, because of nonlinear interaction, and so the typical streamwise slope of the edge is given by

$$\frac{F^*}{L^*} \sim \left(\frac{l^*}{L^*}\right)^{5/6} \text{Re}_w^{-1/6}. \tag{A1}$$

The streamwise slope thus lies between the orders $\text{Re}_w^{-1/6}$ and Re_w^{-1} here. Similarly, the typical spanwise slope F^*/l^*, which is of the order $(l^*\text{Re}_w/L^*)^{-1/6}$ from (A1), lies between the orders unity and $\text{Re}_w^{-1/6}$.

The governing equations in the outer layer are (1) to (3) again but without the viscous terms, and $\tilde{\pi}$ replaces p, while the boundary conditions are in effect $u \sim y + F(x, z)$, $w \to 0$ at large positive y, along with $v \to 0$ as $y \to 0$ for attached motion. The scaling behind

y, F here is as in A1. The above governing equations and constraints, coupled with upstream starting conditions on u, v and w, are to determine the pressure variation $\tilde{\pi}(x, z)$ (and hence B from (8)). As a consequence of the solution behaviour as $y \to 0+$ (which involves square roots), the inner viscous nonlinear layer is quasi-planar in the cross-plane; see in [7]. The streamwise velocity responds linearly and passively. Again, at larger $|z|$ values the outer and inner layers merge into one on top of the roughness [7], while outside the edge there is no nonlinear upstream influence apart from that from $\tilde{\pi}$ via (8) and that produced sideways by momentum spillover downstream [6, 7].

A further discussion of the edge flow solutions that determine $\tilde{\pi}$ can be found in [6, 7] or is available from the authors. An approximation for a nearly straight edge is

$$\tilde{\pi} = -\frac{1}{2}\beta^2 F^2, \qquad\qquad\qquad \text{A2)}$$

where β is the angle between the tangent to the roughness planform and the incident stream direction. This expression matches with properties in [6] for lower roughness heights. Clearly the major variation in $\tilde{\pi}$ occurs within the edge region according to (A2). This quasi-planar solution can be extended to allow for separated eddy flow further downstream (of the roughness) by regarding F as F-effective, defined as the edge height whenever the motion is attached but the eddy height whenever the motion is separated [6, 12]. Here F-effective could be taken to be nearly uniform, consistent with a nearly uniform eddy pressure from (A2). Marginal stability is also mentioned in [7] in connection with these flows.

Appendix B: Linearised analysis

At positions (such as near $x = 0$) where the boundary-layer displacement on a symmetry line $-A(x)$ is small, a linearised analysis of the system (11) to (16) can be performed. Writing $A(x) = \varepsilon a(x)$, where $\varepsilon \ll 1$, the analysis yields for the pressure contribution $P(x)$ and the surface shears $\tau_x = \partial U/\partial y\big|_{y=0}$ and $\tau_z = \partial W/\partial y\big|_{y=0}$ the solutions

$$P(x) \quad = \varepsilon\,\Theta_1 \int_{-\infty}^{x} a''(\xi)(x-\xi)^{-2/3}\mathrm{d}\xi,$$

$$\tau_x - 1 = \varepsilon\,\Theta_2 \int_{-\infty}^{x} a'(\xi)(x-\xi)^{-1/3}\mathrm{d}\xi,$$

$$\tau_z \quad\;\; = \varepsilon\,\Theta_3 \int_{-\infty}^{x} a''(\xi)(x-\xi)^{-1/3}\mathrm{d}\xi,$$

where the constants

$$[\Theta_1, \Theta_2, \Theta_3] = \left[-\frac{3^{2/3}}{\Gamma^2(1/3)}, \frac{3^{1/3}}{\Gamma^2(2/3)} - \frac{2\pi\,3^{-1/6}}{\Gamma(2/3)\Gamma^2(1/3)}, \frac{2\pi\,3^{-1/6}}{\Gamma^2(1/3)\Gamma(2/3)}\right].$$

The linearised solution indicates that unless a smooth start with $a''(x)$ continuous is imposed, singular behaviour in both $P(x)$ and τ_z of the form $x^{-2/3}$ and $x^{-1/3}$ is predicted.

If $a(x) \sim \sigma x$ as $x \to \infty$, then the flow field will become fully nonlinear further downstream where $x = \varepsilon^{-3/2}X$ with X of $O(1)$. A, U, V, W, P and y are rescaled by ε^m, $m = -1/2, -1/2, 1/2, 1, 2$ and $-1/2$ respectively and the governing system becomes (11) to (13) with boundary conditions (14) to (16); $A(x)$ is already in its asymptotic form (10).

References

1. R. Sedney, A survey of the effects of small protuberances on boundary layer flows. *AIAA J.* 11 (1973) 782–792.
2. H. A. Panofsky, The atmospheric boundary layer below 150 metres. *Ann. Rev. Fluid Mech.* 6 (1974) 147–177.
3. A. G. Walton and F. T. Smith, Concerning three-dimensional flow past a tall building on flat ground. *Q. J. Mech. Appl. Math.* 50 (1997) 97–128.
4. W. A. Woods and D. G. Clark, *Visualized Flow (compiled by Japan Soc. Mech. Engs)*. Oxford: Pergamon Press (English translation) (1988) 137 pp.
5. M. Van Dyke, *An Album of Fluid Motion*. Stanford: Parabolic Press (1982) 174 pp.
6. F. T. Smith and A. G. Walton, Flow past a two- or three-dimensional steep-edged roughness. *Proc. R. Soc. London* A 454 (1998) 31–69.
7. F. T. Smith, On physical mechanisms in two- and three-dimensional separations. *Phil. Trans. R. Soc. London* A 358 (2000) 3091–3111.
8. G. B. Ngo Boum, S. Martemianov and A. Alemany, Computational study of laminar flow and mass transfer around a surface-mounted obstacle. *Int J. Heat and Mass Transfer* 42 (1999) 2849–2861.
9. R. Martinuzzi and C. Tropea, The flow around surface-mounted prismatic obstacles placed in a fully developed channel flow. *ASME J. Fluids Eng.* 115 (1993) 85–91.
10. C. J. Baker, The oscillation of a horseshoe vortex system. *ASME J. Fluids Eng.* 113 (1991) 489–495.
11. F. T. Smith, Pipeflows distorted by non-symmetric indentation or branching. *Mathematika* 23 (1976) 62–83.
12. F. T. Smith and P. G. Daniels, Removal of Goldstein's singularity at separation in flow past obstacles in wall layers. *J. Fluid Mech.* 110 (1981) 1–37.
13. F. T. Smith, Flow through symmetrically constricted tubes. *J. Inst. Maths. Applic.* 21 (1978) 145–156.
14. N. C. Ovenden, *The Effect of Increasing Localised Suction on a Boundary Layer and the Generation of Horseshoe Vortices*. Ph.D. thesis, University of London (2001) 322pp.
15. C. W. Jones and E. J. Watson, Two-dimensional boundary layers. In: L. Rosenhead (ed.), *Laminar Boundary Layers*. Oxford: Oxford University Press (1963) pp.198–257.
16. K. Stewartson and P. G. Williams, Self-induced separation II. *Mathematika* 20 (1973) 98–108.
17. F. T. Smith, A three-dimensional boundary-layer separation. *J. Fluid Mech.* 99 (1980) 185–224.